A Quantitative Interpretation of the Response of Articular Cartilage to Atomic Force Microscopy-Based Dynamic Nanoindentation Tests

Matteo Taffetani[1]
MOX, Politecnico di Milano and Fondazione CEN–Centro Europeo di Nanomedicina,
Piazza Leonardo da Vinci, 32,
Milano 20133, Italy
e-mail: matteo.taffetani@polimi.it

Roberto Raiteri[1]
Department of Informatics, Bioengineering, Robotics, and System Engineering,
Università di Genova,
via Opera pia, 13,
Genova 16145, Italy
e-mail: roberto.raiteri@unige.it

Riccardo Gottardi
Ri.MED Foundation,
Palermo 90133, Italy;
Department of Orthopaedic Surgery,
University of Pittsburgh,
Pittsburgh, PA 15260
e-mail: RIG10@pitt.edu

Dario Gastaldi
Department of Chemistry, Materials and Chemical Engineering,
Politecnico di Milano,
Piazza Leonardo da Vinci, 32,
Milano 20133, Italy
e-mail: Dario.gastaldi@polimi.it

Pasquale Vena
Mem. ASME
Department of Chemistry Materials and Chemical Engineering,
Politecnico di Milano,
Piazza Leonardo da Vinci, 32,
Milano 20133, Italy;
IRCCS—Istituto OrtopedicoGaleazzi,
P.zzaR.Galeazzi4,
Milano 20161, Italy
e-mail: pasquale.vena@polimi.it

1 Introduction

AC is a specialized connective tissue that covers the surfaces of diarthrodial joints. Its principal function is to facilitate the transmission of loads while allowing for a low friction [1].

Structurally, chondrocytes generate a porous extracellular matrix, where a network of mainly type II collagen and proteoglycans is present, which is saturated by physiological fluid. The fibrils in the collagen network exhibit a depth-dependent preferred orientation along the thickness: In the superficial layers, the fibers are mainly aligned parallel to the surface; in the deepest layers, they are mainly perpendicular to the bone surface; in the middle region, the distribution is random [2]. Proteoglycans, instead, due to their negative charges, attract water, opposing the fluid flow and thus defining the swelling properties of the tissue [3]. This particular structure, inhomogeneous and anisotropic, determines the unique mechanical properties of the tissue as shown, for example, by Schinagl et al. [4], who evaluated the changes in mechanical properties along the thickness direction, or by Appleyard et al. [5], who analyzed the dependence of such properties on the position on the articular surface. Moreover, the mechanical response of AC is time- and history-dependent. This is mainly due to the interplay between viscoelasticity and poroelasticity that are the two major dissipation mechanisms arising from: (i) the conformational changes of the solid structure and (ii) the fluid flow through the porous microstructure. Viscoelasticity is an intrinsic tissue property, independent from the characteristic length scale analyzed [6]; poroelasticity, on the contrary, is an extrinsic tissue property which depends also on the length scale of the experiments [7].

With the perspective of clinical applications, the interest toward the identification of meaningful correlations between mechanical properties and pathological conditions in AC is high. There is currently a strong effort on mechanical characterization of AC at the micro- and nanoscale [8,9] because, at the smaller scales, it is possible to (a) discriminate between cartilage compo-nents and potentially address biochemical degeneration/healing processes at an early stage and (b) perform tests on small tissue biopsies for ex vivo assays and, eventually, operate in vivo, using miniaturized testing devices, in a minimally invasive way.

[1]Corresponding author.
Manuscript received December 9, 2014; final manuscript received March 15, 2015; published online June 2, 2015. Assoc. Editor: Amir Abbas Zadpoor.

Among the different proposed methodologies for testing AC [10,11], the following ones present interesting aspects for its investigation at the micro- and nanoscale:

(i) Atomic force microscopy (AFM) based nanoindentation test [12,13]. It is extensively used for its simplicity, little need of sample preparation, small volume of sample required, nondestructive operation, and the possibility to investigate samples in liquid environment. Hence, this approach might be implemented into novel diagnostic tools and it has been already employed on AC in a parameter identification process [14].

(ii) Dynamic mechanical analysis (DMA). In DMA, a harmonic stimulus over a range of frequencies is applied to the surface of a sample and the harmonic response is recorded: The frequency dependent properties of the tissue can be extracted from the information on the amplitude of the output signal and the phase shift between the input and output signals [15].

Coupling AFM-based nanoindentation and DMA techniques for the mechanical characterization of soft hydrated tissues has already proved its potential, but it is still an open field of research with many challenges. In fact, as reported in the work of Han et al. [16], this methodology allows for sweeping a wide range of frequencies, collecting much more information than a quasi-static nanoindentation test. Nevertheless, well calibrated systems, capable to provide good signal to noise ratios and to deal with drifting phenomena, are required.

The aim of this paper is to provide a quantitative mechanical interpretation of AFM-DN tests, performed with a micrometric spherical tip (radius $R = 7.5\ \mu$m) over a frequency range from 0.5 Hz to 200 Hz on the superficial layer of AC, using finite ele-ment models to relate the tissue response with respect to relevant parameters such as tissue permeability, anisotropy ratio, and collagen fibrils spatial orientation. Therefore, suitable constitutive equations for the drained properties of the tissue are introduced.

The mechanical parameters are identified through a trial-and-error procedure by matching experimental and numerical results. First, a finite element model of AFM-DN test on a poroelastic material is briefly described. Then, a validation of the AFM-DN simulation is obtained by assuming an elastic transversely isotropic material as presented in Taffetani et al. [17]. This result provides mechanical parameters directly comparable with data already available in literature. Afterwards, the simplified tissue model is replaced with a more realistic one that considers also a continuous fibril distribution [18]; a second identification process is then performed in order to obtain a comprehensive description of the analyzed tissue thickness ($\sim 1.2\ \mu$m).

2 Methods

2.1 AFM-DN Test: Experimental Procedure. Bovine AC samples from skeletally mature animals (2 year old) were harvested from disarticulated femurs (proximal condyles) within 1–2 hr postmortem from a local slaughterhouse using a biopsy punch with 2 mm inner diameter. Each explanted plug consisted of a full-thickness AC fragment with its underlying subchondral bone. The plugs were transferred into phosphate-buffered saline (PBS) (2.6 mM NaH_2PO_4, 3 mM Na_2HPO_4, 155 mM NaCl, 0.01% NaN_3 w/v, *p*H 7.0) supplemented with 20 μg/ml of gentamicin and a protease inhibitor cocktail (P8340, Sigma, St. Louis, MO), and were kept in ice until measurement. Samples were prepared as previously described in Stolz et al. [9] by gluing the base of the plug (the side of the subchondral bone) onto a round petri dish with Histoacryl (B. Braun Surgical GmbH), and fully submerged in PBS throughout testing. Measurements were performed on the same day, within hours from harvest.

Dynamic indentation tests were performed with a commercial AFM (Agilent Technologies 5500, Agilent Technologies, Santa Clara, CA) equipped with a closed loop scanner. A silicon nitride, tipless, rectangular microcantilever (NSC12, MikroMasch, Tallin, Estonia) was employed. The cantilever spring constant k_c was determined to be 7.18 N/m using the so-called "thermal noise method" [19]. A borosilicate glass microsphere with a nominal radius of $R = 7.5\ \mu$m (SPI Supplies, West Chester, PA) was glued onto the free end of the cantilever with a small drop of epoxy resin (Epicote 1004, Shell Chemicals, London, UK) using the translation stage of an optical microscope as described in detail in Raiteri et al. [20]. All experiments presented in this work were performed with the same spherical indenter; after each test, the cantilever at the spherical tip was washed in ethanol and rinsed in PBS.

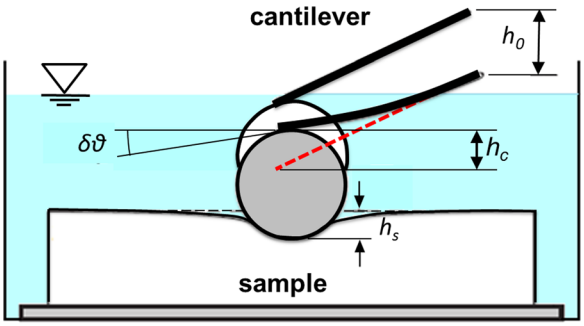

Fig. 1 Schematic side-view of the AFM-DN setup representing the microcantilever, the spherical indenter, and the soft sample. The controlled displacement of the fixed end of the cantilever (h_0), the cantilever deflection (h_c), and the indentation depth (h_s) are reported.

A schematic drawing of the AFM-DN test is reported in Fig. 1. The experiments were performed in two steps.

In the first step, the indentation depth h_s was reached by applying a quasi-static load P via the controlled displacement of the fixed end of the cantilever h_0, which is measured by the capacitive sensors of the AFM scanner. According to the theory of the spherical indentation of a purely elastic isotropic half-space (Hertzian contact theory), the static load–indentation ($P - h_s$) relationship is [21,22]

$$P = \frac{4}{3} E^* \sqrt[2]{R} h_s^{3/2} \tag{1}$$

where $E^* = E/(1-\nu^2)$ is the quasi-static indentation modulus of a deformable body of Young's modulus E and Poisson's ratio ν, while R is the radius of the indenter. This solution is based on the hypothesis that elastic displacements of a plane surface above and below the circle of contact are equal for the whole elastic loading process; thus Eq. (1) holds for $h_s \ll R$.

The cantilever is assumed to have a linear elastic behavior, such that $P = k_c h_c$, where h_c is the cantilever deflection which is measured optically with subnanometer resolution by the AFM.
The indentation depth h_s (also called "mean indentation depth" in the following) can be calculated from the following additive decomposition of the displacement (Fig. 1):

$$h_0 = h_c + h_s \tag{2}$$

In the second step a harmonic displacement $\Delta h_0(f)$ was applied at the fixed end of the cantilever. This signal is characterized by a defined frequency f in the range $[0.5 - 200\,\text{Hz}]$ and an amplitude of 10 nm. The cantilever free end in contact with the sample deflects with a harmonic oscillation at the same frequency f, but with a damped amplitude $\Delta h_c(f)$ and with a phase lag $\phi_f(f)$. Both the amplitude ratio $R^{i/o}(f) = (\Delta h_c(f)/\Delta h_0(f))$ and the phase lag $\phi_f(f)$ are recorded as a function of the frequency.

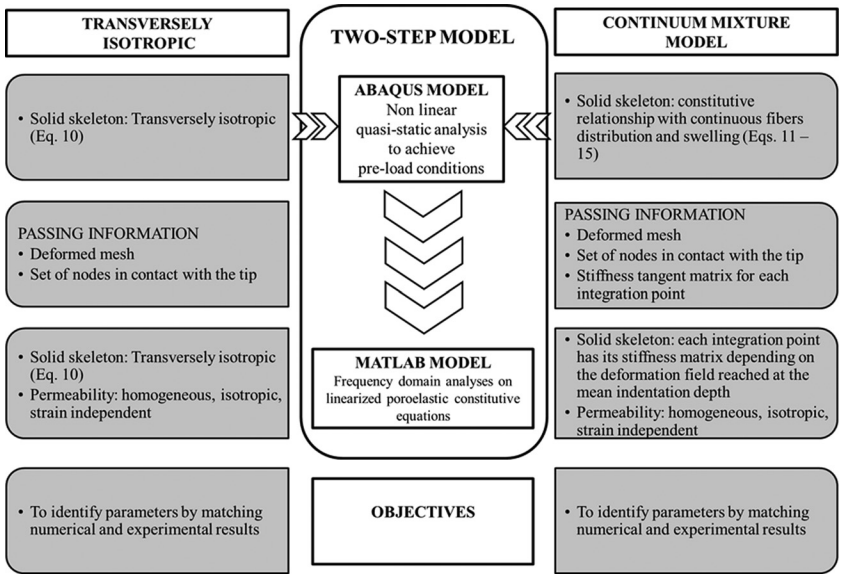

Fig. 2 Overview of the numerical approach based on two models working in sequence and described in the central column: the ABAQUS model, where the equilibrium indentation depth is reached through a nonlinear simulation, and the MATLAB model, where the harmonic displacement is applied using a linearized constitutive relationship. The lateral columns report the AC constitutive equations used to feed the models: the transversely isotropic model and the continuum mixture model, respectively. It is worth noting that, for both the constitutive relationships, the two steps share the same mesh; in the case of the continuum mixture model, also the stiffness tangent matrix obtained at the end of the ABAQUS step is passed to the integration points in the MATLAB step.

Assuming that the cantilever operates within its linear range for all the frequencies analyzed, the harmonic force amplitude $\Delta P(f)$ is related to the harmonic cantilever deflection amplitude $\Delta h_c(f)$ by

$$\Delta P(f) = \Delta h_c(f) k_c \tag{3}$$

Furthermore, additive decomposition can be considered also for the harmonic displacements as

$$\Delta h_0(f) = \Delta h_s(f) + \Delta h_c(f) \tag{4}$$

and finally the ratio between the force amplitude and the indentation amplitude can be related to the amplitude ratio as

$$\frac{\Delta P(f)}{\Delta h_s(f)} = \frac{k_c \Delta h_c(f)}{\Delta h_0(f) - \Delta h_c(f)} = \frac{k_c R^{i/o}(f)}{1 - R^{i/o}(f)} \tag{5}$$

In this work, the AC dynamic response was investigated at three different mean indentation depths $h_s = [1200, 920, 500]$ nm. Dynamic measurements have been performed on three different AC plugs, selecting randomly three different positions for each plug surface: Therefore, from each mean indentation depth nine different measures are averaged. For each plug, before the dynamic measurements, several quasi-static indentation curves (a grid of 1024 curves) were recorded and averaged. This allows to calculate the cantilever deflections h_c, and consequently the applied loads P required to reach the desired indentation depths h_s. For the indentation depths considered in this work $h_s = [1200, 920, 500]$ nm, the corresponding deflections and applied loads were, on average, $h_c = [70, 35, 7]$ nm and $P = [503, 251, 50]$ nN, respectively. After letting the system reach the equilibrium at the desired indentation depth h_s, the sinusoidal vertical displacement was applied while recording the cantilever deflection response using a D/A–A/D board and a custom software developed in LABVIEW (National Instruments, Austin, TX).

2.2 AFM-DN Test: Numerical Simulations. The AFM-DN test has been simulated by a two-step numerical procedure with the following geometrical configuration: A rigid, spherical indenter of radius $R = 7500$ nm was pressed over a cylindrical sample of radius $W = 150$ μm and height $B = 92$ μm. In the first step, a drained (quasi-static) nanoindentation has been simulated to determine the equilibrium conditions upon application of the preload, prior to the cyclic loading phase of the experiment; in the second step, a frequency domain analysis has been developed, simulating the dynamic loading phase.

The first step was performed using the commercial displacement-based finite element code ABAQUS 6.10 (Simulia, Providence, RI) in which the sample is discretized using a 35,000 axisymmetric linear element (CAX4) with a biased, denser mesh under the tip. The second step was performed by means of MATLAB code (MathWorks, Natick, MA).

The finite element analysis carried out in the first step (ABAQUS step) provided the geometry of the deformed domain of the tissue/indenter system upon the application of the preload to reach the mean indentation depth at equilibrium. The analyses were performed using nonlinear anisotropic constitutive equations. In particular, two cases will be discussed: (i) a transversely isotropic constitutive model and (ii) a continuum mixture model with distinct collagen and glycosaminoglycan elastic constituents [18].

In the second step (MATLAB step), the frequency analyses were performed on the deformed domain obtained from the simulation in the first step, and the harmonic displacement was applied on the set of nodes that are in contact with the tip at the end of the first step. The frequency domain analyses were performed in a linearized framework for a fully saturated anisotropic solid [17]; therefore, linear constitutive equations for the solid phase are used. Then, the two cases investigated in the first step become: (i) a transversely isotropic linear constitutive model [17] and (ii) a point-wise anisotropic stress–strain linear response obtained by storing the stiffness matrix of the nonlinear constitutive model implemented in the first step. To this purpose, the analyses of both

steps were carried out using the same finite element mesh and therefore the same integration point locations.

Figure 2 shows a schematic representation of the two modeling steps and how they are performed.

A brief summary of the frequency domain analyses and of the above mentioned constitutive equations is reported below. A description of the experimental data analysis and the identification procedure will close the Sec. 2.

2.3 Numerical Implementation of Harmonic Loading on a Poroelastic Medium. Let us consider a representative volume element (RVE) of volume Ω and boundary Γ of a poroelastic medium. According to the poroelastic theory for the modeling of soft hydrated tissues [23], and assuming the hypotheses of small strains, hydrostatic fluid stresses, isothermal process, and total fluid saturation, the constitutive equations can be written as

$$\begin{cases} \boldsymbol{\sigma} + \alpha \mathbf{m} p = \mathbf{C}^{\mathrm{d}} \boldsymbol{\varepsilon} \\ \dot{\xi} = \alpha \mathbf{m} \dot{\boldsymbol{\varepsilon}} + \dfrac{\dot{p}}{M} \end{cases} \tag{6}$$

where Voigt notation is used, $\boldsymbol{\sigma}$ is the total Cauchy stress vector, p the fluid pressure, $\boldsymbol{\varepsilon}$ the total deformation vector, $\dot{\xi}$ the total variation of fluid content, $\boldsymbol{C}^{\mathrm{d}}$ the elastic drained stiffness tensor, $\boldsymbol{m} = [111000]$, $1/M = n/K_{\mathrm{F}} + (\alpha - n)/K_{\mathrm{S}}$ is the Biot modulus, and $\alpha = 1 - \left(\boldsymbol{m}^{\mathrm{T}} \boldsymbol{C}^{\mathrm{d}} \boldsymbol{m}/9K_{\mathrm{S}}\right)$ is the Biot coefficient. Moreover, n defines the porosity, K_{S} the bulk modulus of the solid matrix, and K_{F} the bulk modulus of the fluid phase. Only the case of incompressible solid part and incompressible fluid part is considered in this work and this assumption implies $1/M = 0$ and $\alpha = 1$.

Under the hypotheses of absence of inertial and body forces, and recalling $\boldsymbol{f}$ as the surface forces, the equilibrium equations on the RVE reduces to

$$\begin{cases} \mathrm{div}(\boldsymbol{\sigma}) = 0 \text{ in } \Omega \\ \boldsymbol{\sigma} \mathbf{n}_{\mathbf{n}} = \mathbf{f} \text{ in } \boldsymbol{\Gamma}_l \end{cases} \tag{7}$$

where div defines the divergence operator in spatial configuration and n_n is the outward normal to the boundary Γ_l of the domain.

Under the hypotheses of a fluid flow regulated by Darcy's law and an isotropic and homogeneous isotropic permeability k, the continuity equation on the RVE can be written as

$$k\,\mathrm{div}(\mathrm{grad}(p)) = \boldsymbol{m}^{\mathrm{T}} \dot{\boldsymbol{\varepsilon}} \tag{8}$$

where grad indicates the gradient operator in spatial configuration.

The aforementioned equations can be implemented into a finite element code using the Galërkin approach to derive their weak formulation. The unknowns are the displacement $\boldsymbol{u}$ and the pressure p. A discretization in finite elements of the whole region Ω is introduced and the harmonic displacement $\bar{\boldsymbol{U}}$, of prescribed amplitude $\boldsymbol{U}_0$ and frequency f, is forced on the node set describing the contact as $\bar{\boldsymbol{U}} = \boldsymbol{U}_0 e^{\mathrm{ift}}$. Therefore, the following linear system can be derived as presented in Taffetani et al. [17]:

$$\begin{bmatrix} \boldsymbol{K}_{uu} & -\boldsymbol{G}_{up} \\ \\ if\boldsymbol{G}_{pu} & -\boldsymbol{K}_{pp} \end{bmatrix} \begin{bmatrix} \boldsymbol{U}_{\mathrm{node}} \\ \\ \boldsymbol{P}_{\mathrm{node}} \end{bmatrix} = \begin{bmatrix} \boldsymbol{F}_u \\ \\ \boldsymbol{F}_p \end{bmatrix} \tag{9}$$

where $\boldsymbol{U}_{\mathrm{node}}$ and $\boldsymbol{P}_{\mathrm{node}}$ are the nodal unknowns (in general, complex numbers). Matrices $\boldsymbol{K}_{uu}$, $\boldsymbol{G}_{up}$, $\boldsymbol{G}_{pu}$, and $\boldsymbol{K}_{pp}$ are built from the constitutive equations, using connectivity and shape functions matrices. Vectors $\boldsymbol{F}_u$ and $\boldsymbol{F}_p$ are known.

2.4 Constitutive Relationships for AC Solid Porous Component

2.4.1 Transversely Isotropic Elastic Material. In a cylindrical reference system, the compliance matrix for the transversely isotropic elastic material C_{ti} is written as

$$\boldsymbol{C}_{\boldsymbol{ti}} = \frac{1}{E_{\mathrm{a}}} \begin{bmatrix} \lambda & -\nu & -\lambda\eta & 0 \\ -\nu & 1 & -\nu & 0 \\ -\lambda\eta & -\nu & \lambda & 0 \\ 0 & 0 & 0 & \dfrac{E_{\mathrm{a}}}{G} \end{bmatrix} \tag{10}$$

The "in-plane" contribution (letter "t" for transversal) is described by the radial and circumferential directions whereas the "out-of-plane" contribution is related to the axial (through the thickness) direction (subscript "a" for axial). Therefore, $\lambda = E_{\mathrm{a}}/E_{\mathrm{t}}$ is the anisotropy ratio, η is the in-plane Poisson's ratio and ν is the out-of-plane Poisson's ratio, E_{a} is the Young's modulus in the axial direction, E_{t} is the Young's modulus along the transverse direction, and G is the shear modulus.

2.4.2 Continuum Mixture Model With Collagen and Glycosaminoglycan Components. The elastic model presented in Taffetani et al. [18] is briefly recalled in this section with the purpose of explaining the meaning of the mechanical parameters that are evaluated in the identification process.

In this model, a continuous fiber distribution $\rho(\theta)$ is assumed. In an axisymmetric framework, $\rho(\theta)$ is defined as

$$\rho(\theta) = \left[\left(\frac{\sin(\theta)}{A} \right)^2 + \left(\frac{\cos(\theta)}{C} \right)^2 \right]^{-\beta} \tag{11}$$

where $A = \tilde{a} V^{\beta/2}$, $C = \tilde{c} V^{\beta/2}$, with $\tilde{a}^{-\beta}$and $\tilde{c}^{-\beta}$ is the semi-axes of the ellipsoidal distribution and β generalizes the description proposed in Ateshian et al. [24]; the angle $\theta \in [0 - \pi]$ sweeps the longitudinal direction. V is the volume of a spherical representative element of unit radius.

The model takes into account the contributions of matrix, collagen, and proteoglycans. Therefore, a stress–strain relationship has to be provided for all the constituents.

The matrix is modeled as a compressible isotropic material; in reference configuration, the second Piola–Kirchhoff matrix stress tensor $\boldsymbol{S}^{\mathrm{MAT}}$ can be written as [25]

$$\boldsymbol{S}^{\mathrm{MAT}} = \mu\left(\boldsymbol{I} - \boldsymbol{C}^{-1}\right) \tag{12}$$

where μ is a material elastic constant for the matrix, $\boldsymbol{I}$ the identity tensor and $\boldsymbol{C} = \boldsymbol{F}^{\mathrm{T}}\boldsymbol{F}$ the right Cauchy–Green with $\boldsymbol{F}$ being the deformation gradient tensor of the map between the material and spatial configurations. The second Piola–Kirchhoff stress tensor $\boldsymbol{S}^{\mathrm{GAGs}}$ related to glicosaminoglycans can be derived as [25]

$$\boldsymbol{S}^{\mathrm{GAGs}} = -\frac{\widehat{\alpha_1}}{J^{(\alpha_2 - 1)}} \boldsymbol{C} \tag{13}$$

where $\widehat{\alpha_1}$ and α_2 are two constitutive parameters and J is the Jacobian of $\boldsymbol{F}$. The contribution of the whole distribution of collagen $\rho(\theta)$ is considered in the following integral:

$$\boldsymbol{S}^{\mathrm{COL}} = \int_{V_s} \bar{S} \tilde{H}(\boldsymbol{n}) \rho(\theta) \boldsymbol{n}(\theta, \varphi) \otimes \boldsymbol{n}(\theta, \varphi) dV \tag{14}$$

where $\bar{S} = \gamma n_H n_K E_{HK}$ is the fiber stress along direction $\boldsymbol{n}$, with E_{HK} the component of the Green Lagrange strain tensor $\boldsymbol{E} = (1/2)(\boldsymbol{C} - \boldsymbol{I})$ and n_H and n_K the components of the direction vector $\boldsymbol{n}$. A modified heaviside function $\tilde{H}(\boldsymbol{n})$is used to smooth the transition between a stretched condition, where the fibers along direction $\boldsymbol{n}$ contribute to $\boldsymbol{S}^{\mathrm{COL}}$, and a compressed condition, where fibers do not contribute to $\boldsymbol{S}^{\mathrm{COL}}$: In particular, $\tilde{H}(\boldsymbol{n}) = 0$ if $n_H n_K E_{HK} < 0$; $\tilde{H}(\boldsymbol{n}) = 1$ if $n_H n_K E_{HK} > 0.01$; a squared cosine function is used in between. The generic direction $\boldsymbol{n}$ can be written as

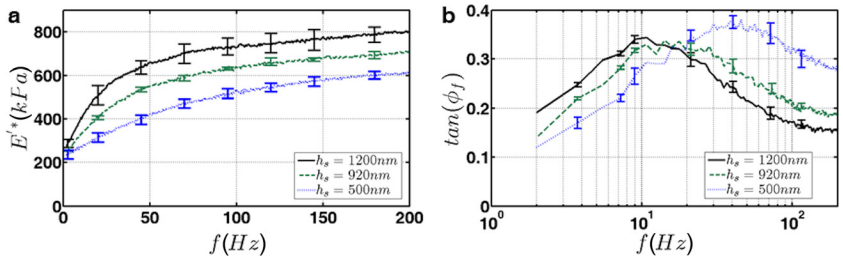

Fig. 3 Experimental data in terms of (*a*) the storage modulus versus frequency and (*b*) the tangent of the phase shift versus frequency for the three indentation depths analyzed. Mean values and standard deviation bars are plotted.

$$\boldsymbol{n} = \begin{bmatrix} \sin(\theta)\cos(\varphi) \\ \cos(\theta) \\ \sin(\theta)\sin(\varphi) \end{bmatrix} \tag{15}$$

where the angle $\varphi \in [0 - 2\pi]$ sweeps the plane of symmetry.

This nonlinear constitutive law is used in the quasi-static finite element simulation in the first step of the numerical analysis. Furthermore, the stiffness tangent matrix, which linearizes the stress–strain relationship described by Eqs. (12)–(14), as obtained at each integration point, is used in the frequency domain simulation of the second step. To this purpose, the tangent stiffness matrix is derived as reported in the appendix of Stender et al. [25].

2.5 Experimental Data Analysis. As explained in Sec. 2.1, the data obtained from the experiments are the amplitude ratio $R^{i/o}(f)$ and the phase lag $\phi_f(f)$. From these, several quantities can be computed and used to characterize the mechanical behavior of the tissue to evaluate the effect of both the geometrical parameters of the experiments and the constitutive parameters of the material.

The reduced storage modulus $E'^*(f)$ and reduced loss modulus $E''^*(f)$ [26] allow to estimate the elastic and the dissipative contribution of the tissue response.

The effects of geometrical parameters can be highlighted by the normalized storage modulus $\bar{E}'^* = (E'^*(f) - E'^*(0))/(E'^*(f \to \infty) - E'^*(0))$, where $E'^*(0)$ and $E'^*(f \to \infty)$ describe the drained and undrained conditions, respectively.

The effect of tissue properties can be studied, instead, by making use of the undrained to drained ratio, $E'^*(f \to \infty)/E'^*(0)$, or through the tangent of the phase shift, $\tan(\phi_f)$, that shows how the porosity affects the overall frequency response and gives an estimation of the typical time scale in which fluid flow mainly occurs.

We base our analysis on two of the aforementioned quantities: (i) the experimental reduced storage modulus $E'^*(f)$ computed as [26]

$$E'^*(f) = \frac{1}{2}\frac{1}{\sqrt[2]{Rh_s}}\left|\frac{\Delta P(f)}{\Delta h_s(f)}\right|\cos(\phi_f(f)) \tag{16}$$

and (ii) the tangent of the phase shift, $\tan(\phi_f)$.

2.6 Parameters Identification Process. In the case of transversely isotropic modeling of the solid phase, one set of constitutive parameters E_a, G, ν, k, λ] has been obtained for each mean indentation depth. The parameter identification process was carried out through a trial-and-error procedure by matching experimental and numerical results in terms of $E'^*(f)$ and tan ϕ_f. Only the mean curves are considered. The rules that drive the manual procedure are described below, as follows from the extensive parameter sensitivity study presented in Taffetani et al. [17]

- The in-plane Poisson's ratio was set to zero, $\eta = 0$ [28].
- Initial guess for the axial modulus E_a and the shear modulus G was selected on the basis of the drained (low frequency) experimental data.
- Once the axial and shear moduli were fixed, the drained behavior depends only on the out-of-plane Poisson's ratio ν, whereas the undrained behavior on the anisotropy ratio λ.
- The permeability k, assumed isotropic, homogeneous, and strain-independent, was identified by matching the numerical and experimental values of the frequency at peak of $\tan(\phi_f)$.

In the case of the continuum mixture model, the set of geometrical parameters for the fiber distribution [A, C, β] and the constitutive parameters [μ, $\widehat{\alpha_1}$, γ] were identified on the basis of the parameter sensitivity study presented in Taffetani et al. [18] and the constitutive parameter $\alpha_2 = 3.22$ was considered as a given datum from the experimental data described in Buschmann and Grodzinsky [27]. In the present work, the trial-and-error procedure has been conducted by matching the averaged experimental data and the numerical results on $E'^*(f)$ and tan ϕ_f obtained only at $h_s = 500$ nm. Afterwards, the identified parameters were used to simulate the mechanical behavior at the other two indenta-tion depths, and the numerical results were compared with the experimental data to validate the set found.

3 Results

3.1 Experimental Tests. Figure 3 shows $E'^*(f)$ and tan ϕ_f as measured from tests conducted at the three mean indentation depths $h_s = [500, 920, 1200]$ nm. For the sake of clarity, we used a linear scale for the frequency axis in Fig. 3(*a*) and a logarithmic scale in Fig. 3(*b*). Data are presented in terms of the average values (solid lines) and the standard deviations (error bar) computed over the nine measures preformed at each mean indentation depth.

3.2 Transversely Isotropic AC Solid Part. Table 1 presents the constitutive parameters estimated for each of the three inden-tation depths used in the experiments. The storage modulus at zero frequency, simulating the drained conditions, increases with the depth, accordingly with the experimental data. As a measure of the quality of the fitting used to identify the constitutive param-eters, Table 1 presents also the value of R^2 computed for both the plots of the storage modulus and the tangent of the phase shift.

In Figs. 4(*a*) and 4(*b*), both the experimental data and the fitting results are shown. The figure shows that a good fitting of experimental data (only the mean curves are presented) can be achieved by using the sets of parameters reported in Table 1. Although three different sets of elastic parameters have been identified, a mismatch in Young modulus E_a lower than 20% in the three experimental sets has been found for R^2 higher than 0.94.

3.3 Continuum Mixture Model. Table 2 shows the single set of parameters (except for the permeability), denoted as

Table 1 Sets of constitutive parameters identified using the transversely isotropic model for the solid component. Data are presented for the three experimental conditions.

							R^2	
h_s (nm)	E_a (kPa)	G (kPa)	ν	k ($\times 10^{-15}$ m^4/N s)	λ	$E'^*(0)$ (kPa)	$E'^*(f)$	$\tan(\phi_f)(f)$
500	180	90	0.04	2	0.16	222	0.97	0.97
920	150	100	0.05	1.5	0.15	229	0.96	0.96
1200	170	105	0.05	1.3	0.15	256	0.94	0.89

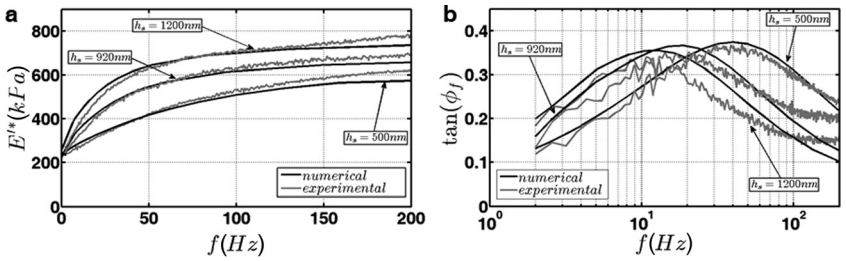

Fig. 4 Best fitting results for all the analyzed experimental data, in terms of (*a*) $E'^*(f)$ and (*b*) $\tan(\phi_f)$ when the transversely isotropic model is used. Data for the three penetration depths are reported: black lines indicate the numerical results and gray lines represent the experimental data (mean curves only).

Table 2 Geometrical and constitutive parameters identified with the continuous fiber distribution model

Model	$\widehat{\alpha_1}$ (MPa)	α_2	μ (MPa)	A	C	β
A_{FIBERS}	0.04	3.32	0.07	3.7	0.007	2.1

A_{FIBERS}, resulting from the trial-and-error procedure applied to the case of mean indentation depth $h_s = 500$ nm. The values of parameters A, C, and β are consistent with those found in Taffetani et al. [18] for the superficial layer of bovine AC, representing a distribution of collagen fibrils mainly oriented parallel to the articular surface. Then, the set of parameters identified for $h_s = 500$ nm has been used to analyze the mechanical behavior at the other two mean indentation depths and the results are presented in Fig. 5. Figure 5(*a*) shows the plot of the experimental data (mean curves only) and the numerical results in terms of the storage modulus and Fig. 5(*b*) in terms of the tangent of the phase shift. The goodness of fit R^2 are: for $h_s = 1200$ nm, $R^2 = 0.85$ for $E'^*(f)$ plot and $R^2 = 0.89$ for $\tan(\phi_f)$ plot; for $h_s = 920$ nm, $R^2 = 0.94$ for $E'^*(f)$ plot and $R^2 = 0.92$ for $\tan(\phi_f)$ plot; and for $h_s = 500$ nm, $R^2 = 0.92$ for $E'^*(f)$ plot and $R^2 = 0.96$ for $\tan(\phi_f)$ plot.

The contribution of permeability is isotropic, homogeneous, and strain-independent also in this second parameter identification process. Therefore, the values found in the first identification procedure remain valid.

4 Discussion and Conclusion

In this work, we propose a novel method for the quantitative estimation of the constitutive parameters for AC, which is achieved by matching the experimental results from AFM-DN tests with the numerical simulations based on frequency domain finite element model. To this end, suitable constitutive equations accounting for tissue anisotropy and for the collagen network architecture have been used. The frequency range investigated in this work (up to 200 Hz) is relevant not only for regular gate but also for sport activities [29], allowing for the characterization of a tissue subjected to loading rates consistent with both regular walk-ing and impact loads.

Two models for the solid component of the tissue have been considered: in the first one, AC is assumed as a transversely isotropic elastic material, whilst in the second one, a constitutive relationship that accounts for a continuous collagen fibril distribution is used. Although the first model does not take into account the fibrous structure of cartilage, it is useful for two reasons: (i)

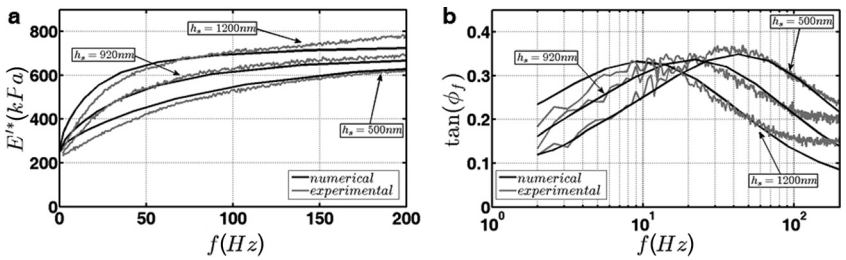

Fig. 5 Best fitting results for all the analyzed experimental data, in terms of (*a*) $E'^*(f)$ and (*b*) $\tan(\phi_f)$ when the fibril distribution model is used. Gray lines define experimental data (mean curves only) whereas black lines indicate the numerical results obtained by using the parameters of model A_{FIBERS}.

the relationships between the mechanical parameters of the model and the outputs of the numerical simulations can be easily extracted via a sensitivity analysis; (ii) the identified parameters can be directly compared with results discussed in the literature [29].

In the work of Han et al. [16], an estimation for the poroelastic characteristic frequency $f_p = Hk/L_p^2$, being H the equilibrium elastic modulus and L_p the characteristic length, is proposed such that, if a range of frequency $f < f_p$ is studied, the material can be correctly assumed as poroelastic. Assuming $H \sim 0.2 - 0.4$ MPa (from Fig. 3(a)), $k \sim 10^{-14} - 10^{-15}$ m^4/Ns [16,30,31], and $L_p \sim 2.6 - 4.3$ μm (from the experimental setup), a value of f_p of the order of tens of Hz can be found. Moreover, noticing that the position of the peaks in Fig. 3(b) changes with h_s, it appears that the material response is affected by a characteristic length of the experiment, consistently with a mainly poroelastic behavior. Our experimental results also show a depth-dependence of the investigated properties consistent with literature evidences as, for example, discussed in Chen et al. [32]: Indeed, both drained and undrained moduli increase with the increase of the mean indentation depth. Besides, different mean indentation depths induce changes in phase shift peak as both its magnitude and its position decrease when the mean indentation depth increases.

On the basis of the sensitivity analysis proposed in Taffetani et al. [17], the model that implements a transversely isotropic elastic material permits to extract some interesting correlations between constitutive parameters and the observed mechanical behavior: Such correlations can be used to drive the trial-and-error procedure. For given axial and shear moduli, the drained behavior is driven by the out-of-plane Poisson's ratio ν only, whereas the undrained modulus is only dependent on the anisotropy ratio λ. Hence, it is possible to separately identify ν and λ. Moreover, both ν and λ affect the phase shift in opposite ways: An increase of λ results in an increase of the maximum of $\tan(\phi_f)$, whereas increasing the magnitude of the parameter ν causes a decrease in the peak value. The frequency of the phase shift peak value is strictly affected by the characteristic time of the poroelastic response of the tissue; this consideration allows for a direct estimation of the tissue permeability.

Although the experiments reported in Nia et al. [30] are performed at a characteristic length smaller than that investigated in this work (~ 1.7 μm versus $2.6 - 4.3$ μm used here) on young bovine AC sample, it is worth comparing the results obtained in our work by modeling AC as a transversely isotropic elastic mate-rial with those found by Nia et al. [30]. In that work, the authors used a fiber reinforced model and a constant value for the Poisson's ratio equal to 0.1 and found the values $E_{m,\mathrm{NIA}} = 0.032$ MPa, $E_{f,\mathrm{NIA}} = 0.29$ MPa, and $k_{\mathrm{NIA}} = 1.3 \times 10^{-14}$ m^4/Ns, for the matrix stiffness, fiber stiffness, and permeability, respectively. Considering that the collagen fibrils are mainly parallel to the surface in the superficial layers, the matrix stiffness $E_{m,\mathrm{NIA}}$ is representative of the axial stiffness, whereas the fiber stiffness $E_{f,\mathrm{NIA}}$of the transver-sal one: the ratio between these two values is around 0.1 which is
very close to the anisotropy ratio $\lambda = 0.15$ calculated in this work. Regarding the permeability, Nia et al. [30] proposed a value that is one order of magnitude lower than the one identified in our procedure. Nevertheless, it has been shown that permeability strongly depends on tissue sources [33] and the characteristic length investigated [31].

The parameters found using the continuum mixture model for the solid part of AC (Table 2) are consistent with those found for the transversely isotropic model. Indeed, similar transverse to axial stiffness ratio as well as similar shear modulus have been found with both models. Moreover, the coefficients describing the fibril distribution are in agreement with those identified in Taffetani et al. [18]. Furthermore, the values of $\hat{\alpha}_1$ found in this study are consistent with the speculation proposed by Ateshian et al. [24] and Lu and Mow [34], in which the fixed charged density c_F on the proteoglycans ranges in between 0.04 mEq/l and 200 mEq/l, corresponding to $\hat{\alpha}_1$ varying from 0.03 MPa and 0.1 MPa [35]. Interestingly, this single set of parameters found for $h_s = 500$ nm is suitable to simulate the dynamic behavior of the tissue at all penetration depths investigated, up to a maximum of $h_s = 1200$ nm, giving a further validation of the goodness of the procedure.

In this work, frequency domain characterization experiments at small scale (AFM-DN) are combined with a comprehensive mechanical constitutive law for AC, for an effective interpretation of the experimental results. Differently from other works, such as Nia et al. [30], this research (i) investigates a larger set of parameters, using also a more realistic description of the tissue, and (ii) evaluates numerically the harmonic loading directly in the frequency domain, in a less computational time consuming approach. The identification procedure, although performed via the manual fitting of experimental results, is able to determine relevant tissue properties of AC. In particular, correctly assumed as tissue permeability and elastic anisotropy can be identified with a single measurement.

The results achieved in this work show the relevance of the combination of frequency domain modeling and microscale characterization experiments for an effective tissue characterization. An extension to clinically relevant applications on engineered tissues substitutes or to diseased tissues can be easily envisioned.

References

[1] Pearle, A., Warren, R., and Rodeo, S., 2005, "Basic Science of Articular Cartilage and Osteoarthritis," Clin. Sports Med., **24**(1), pp. 1–12.

[2] Mankin, H., Mow, V., and Buckwalter, J., 1999, "Articular Cartilage Structure, Composition and Function," *Orthopaedic Basic Science: Biology and Biomechanics of the Musculoskeletal System*, American Academy of Orthopaedic Surgeons, Rosemont, IL, pp. 443–470.

[3] Poole, A., Kojima, T., Yasuda, T., Mwale, F., Kobayashi, M., and Laverty, S., 2001, "Composition and Structure of Articular Cartilage: A Template for Tissue Repair," Clin. Orthop. Relat. Res., **391**(Suppl.), pp. S26–S33.

[4] Schinagl, R., Gurskis, D., Chen, A., and Sah, R., 1997, "Depth-Dependent Confined Compression Modulus of Full Thickness Bovine Articular Cartilage," J. Orthop. Res., **15**(4), pp. 499–506.

[5] Appleyard, R., Burkhardt, D., Ghosh, P., Read, R., Cake, M., Swain, M., and Murrel, G., 2003, "Topographical Analysis of the Structural, Biochemical and Dynamical Biomechanical Properties of Cartilage in an Ovine Model of Osteoarthritis," Osteoarthritis Cartilage, **11**(1), pp. 65–77.

[6] Huang, C., Mow, V., and Ateshian, G., 2001, "The Role of Flow Independent Viscoelasticity in the Biphasic Tensile and Compressive Responses of Articular Cartilage," ASME J. Biomech. Eng., **123**(5), pp. 410–418.

[7] Hu, Y., Zhao, X., Vlassak, J., and Suo, Z., 2010, "Using Indentation to Characterize the Poroelasticity of Gels," Appl. Phys. Lett., **96**(12), p. 121904.

[8] Ebenstein, D., and Pruitt, L., 2006, "Nanoindentation of Biological Materials," Nano Today, **1**(3), pp. 26–33.

[9] Stolz, M., Gottardi, R., Raiteri, R., Miot, S., Martin, I., Imer, R., Staufer, U., Raducanu, A., Duggelin, M., Baschong, W., Daniels, A., Friederich, N., Aszodi, A., and Aebi, U., 2009, "Early Detection of Aging Cartilage and Osteoarthritis in Mice and Patient Samples Using Atomic Force Microscopy," Nat. Nanotechnol., **4**(3), pp. 186–192.

[10] Armstrong, C., Lai, V., and Mow, V., 1984, "An Analysis of the Unconfined Compression of Articular Cartilage," ASME J. Biomed. Eng., **106**(2), pp. 165–173.

[11] Li, C., Pruitt, L., and King, K., 2006, "Nanoindentation Differentiates Tissue-Scale Functional Properties of Native Articular Cartilage," J. Biomed. Mater. Res., Part A, **78**(4), pp. 729–758.

[12] Stolz, M., Raiteri, R., Daniels, A., van Landingham, M., Baschong, W., and Aebi, U., 2004, "Dynamic Elastic Modulus of Porcine Articular Cartilage Determined at Two Different Levels of Tissue Organization by Indentation-Type Atomic Force Microscopy," Biophys. J., **85**(5), pp. 3269–3683.

[13] Loparic, M., Wirtz, D., Daniels, A., Raiteri, R., van Landingham, M., Guex, G., Martin, I., Aebi, U., and Stolz, M., 2010, "Micro- and Nanomechanical Analysis of Articular Cartilage by Indentation-Type Atomic Force Microscopy: Validation With a Gel–Microfiber Composite," Biophys. J., **98**(11), pp. 2731–2740.

[14] Simha, N., Jin, H., Hall, M., Chiravarambath, S., and Lewis, J., 2007, "Effect of Indenter Size on Elastic Modulus of Cartilage Measured by Indentation," ASME J. Biomech. Eng., **129**(5), pp. 767–775.

[15] Franke, O., Goken, M., Meyers, M., Durst, K., and Hodge, A., 2011, "Dynamic Nanoindentation of Articular Porcine Cartilage," Mater. Sci. Eng. C, **31**(4), pp. 789–795.

[16] Han, L., Frank, E., Greene, J., Lee, H., Hung, H., Grodzinsky, A., and Ortiz, C., 2011, "Time-Dependent Nanomechanics of Cartilage," Biophys. J., **100**(7), pp. 1846–1854.

[17] Taffetani, M., Bertarelli, E., Gottardi, R., Raiteri, R., and Vena, P., 2012, "Modelling of the Frequency Response to Dynamic Nanoindentation of Soft Hydrated Anisotropic Materials: Application to Articular Cartilage," Comput. Model. Eng. Sci., **87**(5), pp. 433–460.

[18] Taffetani, M., Griebel, M., Gastaldi, D., Klisch, S., and Vena, P., 2014, "Poroviscoelastic Finite Element Model Including Continuous Fiber Distribution for the Simulation of Nanoindentation Tests on Articular Cartilage," J. Mech. Behav. Biomed. Mater., **32**(1), pp. 17–30.
[19] Hutter, J., and Bechhoefer, J., 1993, "Calibration of Atomic Force Microscope Tips," Rev. Sci. Instrum., **64**(7), pp. 1868–1876.
[20] Raiteri, R., Preuss, M., Grattarola, M., and Butt, H., 1998, "Preliminary Results on the Electrostatic Double Layer Force Between Two Surface With High Surface Potential," Colloid Surf. A, **136**(1–2), pp. 195–201.
[21] Johnson, K., 1985, *Contact Mechanics*, Cambridge University, Cambridge, UK.
[22] Field, J., and Swain, M., 1993, "A Simple Predictive Model for Spherical Indentation," J. Mater. Res., **8**(2), pp. 297–306.
[23] Cowin, S., and Doty, S., 2006, *Tissue Mechanics*, Springer Verlag, New York.
[24] Ateshian, G., Rajan, V., Chahine, N., Canal, C., and Hung, C., 2009, "Modeling the Matrix of Articular Cartilage Using a Continuous Fiber Angular Distribution Predicts Many Observed Phenomena," ASME J. Biomech. Eng., **131**(6), p. 061003.
[25] Stender, M. E., Raub, C. B., Yamauchi, K. A., Shirazi, R., Vena, P., Sah, R. L., Hazelwood, S. J., and Klisch, S. M., 2013, "Integrating qPLM and Biomechanical Test Data With an Anisotropic Fiber Distribution Model and Predictions of TGF-β 1 and IGF-1 Regulation of Articular Cartilage Fiber Modulus," Biomech. Model. Mechanobiol., **12**(6), pp. 1073–1088.
[26] Cheng, Y., Ni, W., and Cheng, C., 2006, "Nonlinear Analysis of Oscillatory Indentation in Elastic and Viscoelastic Solids," Phys. Rev. Lett., **97**(7), p. 075506.
[27] Buschmann, M., and Grodzinsky, A., 1995, "A Molecular Model of Proteoglycan-Associated Electrostatic Forces in Cartilage Mechanics," ASME J. Biomech. Eng., **117**(2), pp. 179–192.
[28] Korhonen, R., Wong, M., Arokoski, J., Lindgern, R., Helminen, H., Hunziker, E., and Jurvelin, J., 2002, "Importance of the Superficial Tissue Layer for the Indentation Stiffness of Articular Cartilage," Med. Eng. Phys., **24**(2), pp. 99–108.
[29] Buckwalter, J., 2002, "Articular Cartilage Injuries," Clin. Orthop. Relat. Res., **402**(1), pp. 21–37.
[30] Nia, H., Han, L., Li, Y., Ortiz, C., and Grodzinsky, A., 2011, "Poroelasticity of Cartilage at the Nanoscale," Biophys. J., **101**(9), pp. 2304–2313.
[31] Lu, X., Wan, L., Guo, X., and Mow, V., 2010, "A Linearized Formulation of Triphasic Mixture Theory for Articular Cartilage and Its Application to Indentation Analysis," J. Biomech., **43**(4), pp. 673–679.
[32] Chen, A., Bae, W., Schinagl, R., and Sah, R., 2001, "Depth- and Strain-Dependent Mechanical and Electromechanical Properties of Full-Thickness Bovine Articular Cartilage in Confined Compression," J. Biomech., **34**(1), pp. 1–12.
[33] Williamson, A., Chen, A., and Sah, R., 2001, "Compressive Properties and Function-Composition Relationships of Developing Bovine Articular Cartilage," J. Orthop. Res., **19**(6), pp. 1113–1121.
[34] Lu, X., and Mow, V., 2008, "Biomechanics of Articular Cartilage and Determination of Material Properties," Med. Sci. Sports Exercises, **40**(2), pp. 193–199.
[35] Chahine, N., Chen, F., Hung, C., and Ateshian, G., 2005, "Direct Measurement of Osmotic Pressure of Glycosaminoglycan Solutions by Membrane Osmometry at Room Temperature," Biophys. J., **89**(3), pp. 1543–1550.